PHYSICAL REVIEW B **110**, 075157 (2024)

Probing surface and bulk ground states of lanthanides: 4f moment orientation through 4d x-ray absorption spectroscopy

D. Yu. Usachov,[1,2,3,*] K. A. Bokai,[1,2] I. I. Klimovskikh,[4] K. Ali,[5] F. Schiller,[6] G. Poelchen,[7]
V. S. Stolyarov,[2,3] K. Kliemt,[8] C. Krellner,[8] and D. V. Vyalikh[4,9,†]
[1]*St. Petersburg State University, 7/9 Universitetskaya nab. St. Petersburg 199034, Russia*
[2]*Moscow Institute of Physics and Technology, Institute Lane 9, Dolgoprudny 141701, Russia*
[3]*National University of Science and Technology MISIS, Moscow 119049, Russia*
[4]*Donostia International Physics Center (DIPC), 20018 Donostia/San Sebastián, Basque Country, Spain*
[5]*Department of Microtechnology and Nanoscience, Chalmers University of Technology, Göteborg 41296, Sweden*
[6]*Centro de Física de Materiales CSIC/UPV-EHU-Materials Physics Center, E-20018 San Sebastián, Spain*
[7]*Institut für Festkörper- und Materialphysik, Technische Universität Dresden, 01069 Dresden, Germany*
[8]*Kristall- und Materiallabor, Physikalisches Institut, Goethe-Universität Frankfurt,*
Max-von-Laue Strasse 1, D-60438 Frankfurt am Main, Germany
[9]*IKERBASQUE, Basque Foundation for Science, 48013 Bilbao, Spain*

(Received 19 July 2024; accepted 14 August 2024; published 27 August 2024)

Knowledge of the ground state of lanthanides (Ln) in Ln-based materials is fundamental for understanding their properties, particularly those related to magnetism. In crystalline materials, the magnitude and orientation of 4f magnetic moments are often strongly influenced by the crystal electric field (CEF), making them challenging to predict *ab initio*. This complexity is intensified in low-dimensional systems and nanostructures, where the CEF may vary significantly near surfaces and at interfaces. The related variations of the 4f ground state should be probed by methods with adjustable surface sensitivity. Here, we apply x-ray absorption spectroscopy (XAS) at the Ln 4d edge, along with modeling of XAS spectra, to probe the 4f ground state of Ln atoms both at the surface and in the bulk of LnRh$_2$Si$_2$ layered crystals. Our results explicitly reveal significant changes of the 4f ground state, which may lead to the reorientation of 4f moments at the surface compared to the bulk, driven by alterations of the CEF. We also provide a comprehensive database of calculated Ln 4d XAS spectra in numeric format for all lanthanides. Our findings will facilitate studies of Ln-based materials and molecular complexes by enabling comprehensive analysis of XAS data, including those obtained through magnetic linear and circular dichroism techniques, as well as related spectromicroscopy studies.

DOI: 10.1103/PhysRevB.110.075157

I. INTRODUCTION

The development of materials containing lanthanides (Ln) represents a rapidly evolving field of research, driven by their diverse applications in areas such as light emission, optical devices, catalysis, biomedical analysis, cell imaging, and beyond [1–5]. Especially, due to their large 4f magnetic moments and significant magnetic anisotropy, lanthanides are attractive for the development of magnetic material systems such as supramolecular complexes [3], molecular magnets [6,7], or multilayered structures and sequences [8], both for fundamental studies and for implementation in magnetically relevant devices, particularly for spintronics and magnetic storage media [9–15].

The magnitude and orientation of the 4f magnetic moments essentially depend on the local environment of the lanthanide atom within the system, particularly influenced by the electric field created by surrounding atoms. Our recent studies have revealed that the orientation of 4f moments at the surface of lanthanide-containing crystals notably differs from that within the bulk [16–18]. As also shown theoretically [19–21], this is caused by alterations in the crystal electric field (CEF) at the surface region. We showed that the respective property can be determined through surface-sensitive 4f photoemission (PE) measurements and analysis of the line shape of the 4f multiplet, which is related to the $|M_J\rangle$ states defining the orientation of the 4f moment [16].

In light of these results, it is reasonable to assume that the mentioned reorientation of the 4f moments can be derived from the x-ray absorption spectroscopy (XAS) measurements performed at the 4d → 4f threshold of the lanthanide atom, which are slightly more surface sensitive as compared to measurements at the 3d → 4f threshold [22–24]. The latter are traditionally considered as mostly bulk sensitive. Moreover, the structure of XAS spectra taken at the 4d threshold of lanthanide atoms is much richer compared to that at the 3d threshold; the spectral features are well separated in energy, making it easier to analyze changes in their relative intensities. We assume that performing the XAS 4d → 4f measurements in both partial and total electron yield (PEY and TEY) modes

---

[*] Contact author: dmitry.usachov@spbu.ru

[†] Contact author: denis.vyalikh@dipc.org

would allow us to emphasize and describe the properties at the surface of the material. It is worth noting that although XAS $3d \rightarrow 4f$ measurements are widely used to investigate magnetic materials, XAS $4d \rightarrow 4f$ studies are relatively rare. This can be explained by the enhanced complexity of modeling of the $4d \rightarrow 4f$ threshold [25]. This complexity is further accentuated for the near-surface Ln atoms due to their distinct coordination and chemical properties in comparison to the bulk, as well as their unique magnetic properties.

The essential advance of XAS experiments at the $4d \rightarrow 4f$ threshold, in comparison to $4f$ photoemission measurements, would also include the opportunity to perform magnetic dichroism experiments in both PEY and TEY modes for rather different material systems including single crystals [18,26], molecular magnets [6], supramolecular complexes [3], and multilayered sequences containing several types of lanthanides. The latter can be challenging to discern from $4f$ PE measurements, since $4f$ multiplets from different sorts of lanthanides may overlap with each other as well as with valence states. Application of the proposed XAS measurements would allow us to obtain useful information about surface and bulk Ln ground states, including the orientation of $4f$ moments.

II. EXPERIMENT

XAS measurements were carried out at the FlexPES beamline of MAX IV, the Swedish national synchrotron radiation facility. The detailed description of FlexPES is reported in Ref. [27]. The analytical chamber of this instrument is equipped with a homebuilt microchannel plate detector with selectable retardation voltage, which we employed for PEY measurements. High quality single-crystalline samples of $\mathrm{LnRh_2Si_2}$, crystallized in the body-centered tetragonal $\mathrm{ThCr_2Si_2}$ structure [28], were cleaved *in situ* in ultrahigh vacuum at a base pressure better than 1×10^{-10} mbar. Si-terminated terraces of cleaved sample were readily detected via ARPES measurements and observation of intense surface state near the $\overline{\mathrm{M}}$ point of the surface Brillouin zone, whereas for Ln termination, the surface state is absent [29–32]. The XAS spectra were acquired using linear horizontal polarization of incoming photons with normal incidence on the sample. The energy resolution was better than 15 meV.

It is essential to note that currently the lowest possible temperature provided by FlexPES for performing XAS measurements is 40 K. At this temperature, only $\mathrm{TbRh_2Si_2}$ was tested in its antiferromagnetic (AFM) phase with a Néel temperature of 94 K. All other $\mathrm{LnRh_2Si_2}$ materials were examined in the paramagnetic (PM) phase. The obtained results indicate that XAS measurements performed in both PEY and TEY modes provide valuable insights into which M_J values contribute to the line shape of XAS spectra in the PM phase. Consequently, our data enable prediction of the orientation of $4f$ moments both at the surface and within the bulk as the system enters the magnetically ordered phase.

III. MODELING

To calculate the XAS cross section, denoted as σ, we consider a single Ln^{3+} ion possessing an electronic configuration of $[\mathrm{Xe}]4f^n$. Our analysis restricts the consideration to final states involving one photoelectron, while neglecting the contribution of spontaneous emission, which is negligible. Thus, σ becomes identical to the photoemission cross section. Next, we assume that total angular momentum J is a good quantum number for the ground state $|g\rangle$, which can be split in electric and/or magnetic field into several states $|g^\nu\rangle$. Thus, they can be expressed as a linear combination of the states $|4f^nJM_J\rangle$ with coefficients $A^\nu_{M_J}$:

$$|g^\nu J\rangle = \sum_{M_J} A^\nu_{M_J} |M_J\rangle. \qquad (1)$$

In most cases, this is a good approximation, although in general different J may become slightly mixed under the influence of CEF and magnetism. The respective cross section is given by

$$\sigma^\nu = \sum_{J'} \sigma_{J'} \frac{3(2J+1)}{2J'+1} \sum_{M'_J} \left| \sum_{qM_J} \varepsilon_q A^\nu_{M_J} C^{J'M'_J}_{JM_J,1q} \right|^2, \qquad (2)$$

where ε_q are the three spherical tensor components of the photon polarization $\{(\varepsilon_x + i\varepsilon_y)/\sqrt{2}, \varepsilon_z, (-\varepsilon_x + i\varepsilon_y)/\sqrt{2}\}$, C denotes the Clebsch-Gordan coefficient and $\sigma_{J'}$ are functions of the photon energy ω (atomic units are used), defined as

$$\sigma_{J'}(\omega) \equiv \frac{1}{3(2J+1)} \sum_f |\langle fJ'||\hat{T}||gJ\rangle|^2, \qquad (3)$$

with $\hat{T}$ being the operator of the transition to the final state f with the total angular momentum J'. The spectra $\sigma_{J'}(\omega)$ are independent on geometry, polarization, or splitting of the ground state. The selection rule $|J' - J| \leqslant 1$ limits the number of these spectra to three (or one with $J' = 1$ when $J = 0$). In the Supplemental Material (SM) [33], we provide in graphical and numeric formats the spectra $\sigma_{J'}$ calculated for all trivalent lanthanides with the aim of simplifying the analysis of experimental XAS data, including x-ray magnetic circular and linear dichroism (XMCD, XMLD) results. Once these spectra are known, one can easily calculate the XAS spectrum $\sigma(\omega)$ for any photon polarization $\vec{\varepsilon}$, temperature T, and ground state specified by the coefficients A^ν and energies E_ν of the split level $|gJ\rangle$, using Eq. (2) and the Boltzmann distribution:

$$\sigma(\omega) = \frac{1}{Z} \sum_\nu \sigma^\nu(\omega) \mathrm{e}^{-E_\nu/kT}, \quad Z = \sum_\nu \mathrm{e}^{-E_\nu/kT}. \qquad (4)$$

Note that for the case of the degenerate ground state (without CEF and magnetism), the spectrum is given by $\sigma = \sum_{J'} \sigma_{J'}$.

In the calculation, we consider direct PE from the $4f$ and $4d$ states and indirect PE, which includes photoexcitation from the ground $4f^n$ configuration to the intermediate $|4f^{n+1}4d^9\rangle$ states, followed by a decay through various channels. We include a super-Coster-Kronig channel with $|4f^{n-1}, kl\rangle$ final states, where kl indicates photoelectron with momentum k and orbital quantum number l, a Coster-Kronig decay to $|4f^n 5(s,p)^{-1}, kl\rangle$ states, where one hole is created in either $5s$ or $5p$ subshell, a decay to $|4f^n 4d^{-1}, kl\rangle$ states, where only $l = 3$ is significant, therefore it can be called f tunneling. We also account for the Auger channel involving final states $|4f^{n+1} 5(s,p)^{-2}, kl\rangle$, where two holes can reside

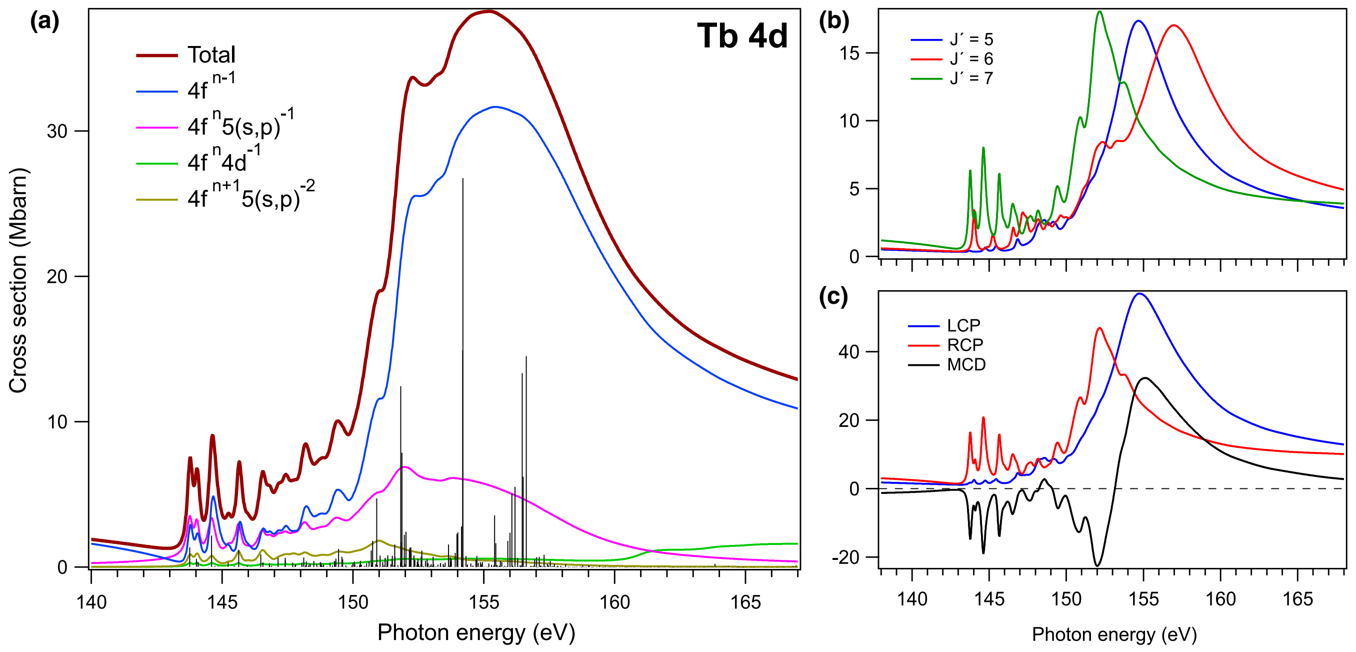

FIG. 1. Theoretical XAS spectra for Tb^{3+} at the $\mathrm{N}_{4,5}$ ($4d \rightarrow 4f$) threshold. (a) Contributions of different decay channels to the XAS spectrum. Vertical lines indicate probabilities of transitions to the intermediate states. (b) Partial XAS spectra, denoted as $\sigma_{J'}$, corresponding to three possible values of the total momentum J' in the final state. (c) Calculated XMCD spectra of Tb magnetized in the direction of the photon source, considering zero temperature and absence of CEF: two spectra for left circularly polarized (LCP) and right circularly polarized (RCP) light, along with their difference (MCD), are shown.

either within one subshell ($5s^0$ or $5p^4$) or in two different subshells ($5s^1 5p^5$). We provide separate contributions of each channel to the XAS spectra that can be useful for interpreting data obtained in PEY mode.

For the transition matrix element in Eq. (3), we use the general formula given in Ref. [25]. Coulomb radial integrals were scaled to obtain good agreement between the calculated spectra and experimental data for LnF_3 compounds [34]. The details and parameters of calculation are given in the SM [33].

IV. RESULTS

As an example of XAS calculation results, we illustrate in Fig. 1(a) the model spectrum for Tb at the $4d$ edge. In general, for most Ln-containing materials the shape of the XAS spectrum at the $\mathrm{N}_{4,5}$ ($4d \rightarrow 4f$) threshold is formed by a fine pre-edge structure at lower photon energies, followed by a broad giant resonance at higher energies [34–40]. The calculated XAS spectrum of Tb is shown together with the contributions from different decay channels labeled in Fig. 1(a). As seen, while almost all considered channels contribute significantly to the pre-edge structure, only the super-Coster-Kronig channel makes the most essential contribution to the giant peak, with a minor contribution from the remaining channels.

Although the spectrum in Fig. 1(a) corresponds to unpolarized ground state without CEF splitting, we provide a possibility to calculate polarized spectra using Eq. (2) together with our precalculated partial spectra $\sigma_{J'}$ given in the SM [33]. For the case of Tb, they are shown in Fig. 1(b). As an example, in Fig. 1(c) we demonstrate model spectra for the magnetically polarized ground states of Tb with $M_J = \pm 6$ and the respective MCD curve that closely resembles the experimental one [41]. It is worth noting that due to the pronounced Fano effect (interference of the direct and resonant PE), the orbital moment projection $\langle L_z \rangle$ determined from the XMCD sum rule [42,43] may slightly deviate from the real one (for Tb it is reduced by $\sim$11%).

To further illustrate our methodology, we focus on the aforementioned family of $\mathrm{LnRh_2Si_2}$ materials [28], which we have already extensively characterized through ARPES [30–32,44] as well as $4f$-photoemission measurements and modeling [16,18]. The layered structure of these materials, where Ln atomic planes are separated by silicide Si–Rh–Si blocks, allows easy cleaving of the sample and obtaining surfaces with large Ln and Si terminations [44].

We begin with the study of the AFM material $\mathrm{TbRh_2Si_2}$ [45]. When it undergoes a transition to the AFM phase below 94 K, the Tb $4f$ moments become ordered ferromagnetically (FM) within each Tb atomic layer, with an out-of-plane orientation [45]. At that, the neighboring layers with FM-ordered Tb $4f$ moments, separated by silicide Si–Rh–Si blocks, are coupled antiferromagnetically along the c axis.

Let us consider XAS spectra for Tb $4d \rightarrow 4f$ absorption threshold, taken in both TEY and PEY modes, together with the results of modeling, summarized in Fig. 2. All experimental spectra (also in Figs. 3 and 4) were scaled in intensity to facilitate comparison of their line shape. The model spectra in Figs. 2, 3, 4, and 5(b) were slightly broadened by convolution with Lorentzian contour with a half-width of 50 meV, aiming to promote better visual comparison with the experimental data. The top two spectra shown in Fig. 2 were obtained from XAS measurements in TEY mode, performed on both Si- and Tb-terminated surfaces of $\mathrm{TbRh_2Si_2}$ (identified with ARPES

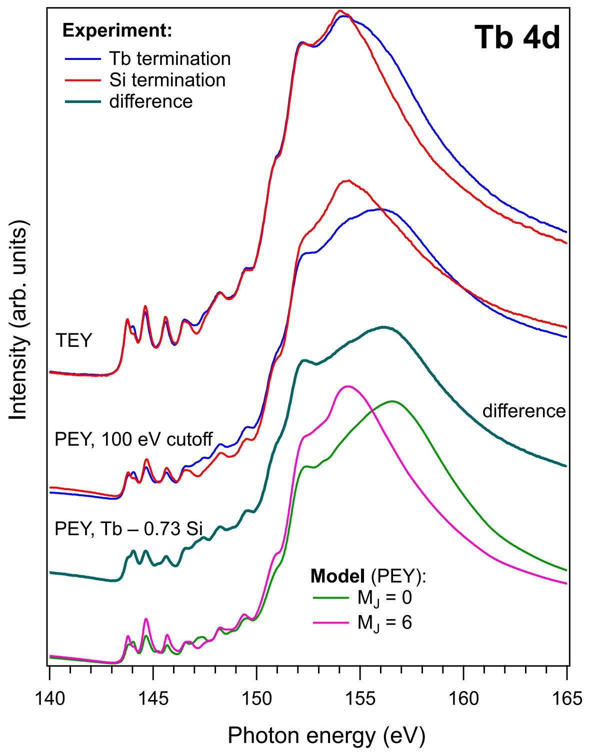

FIG. 2. Experimental XAS Tb $N_{4,5}$ spectra acquired in TEY and PEY regimes from Tb- and Si-terminated surfaces of AFM-ordered $TbRh_2Si_2$, compared with theoretical spectra for two hypothetical ground states $|0\rangle$ and $|6\rangle$ of Tb.

through observation of the surface states [30]). Comparing them, we conclude that while small differences can be seen for the pre-edge structure, the most essential distinction is observed at the photon energies above 152 eV, in the region of giant resonance. Further, we enhance the surface sensitivity of XAS measurements by applying a retarding voltage of 100 V. In this case, the electrons with kinetic energy smaller than the applied voltage are not detected, and only fast electrons escaping from the near-surface region without inelastic scattering contribute to the measured signal. The respective two PEY spectra taken from the Si and Tb surfaces are depicted in the middle of Fig. 2. As seen, the differences in the giant resonance become much more prominent now and, additionally, certain distinctions become visible in the pre-edge structure.

To model the PEY XAS spectra, it is essential to remember that the $4f$ PE measurements indicate a strong reorientation of the magnetic $4f$ moments at the Tb surface in comparison to the bulk [16]. As mentioned, this is caused by the change of CEF at the surface. Therefore, we performed modeling for hypothetical states with $M_J = 0$ and $M_J = 6$, which imply in-plane and out-of-plane orientations of the Tb $4f$ moments, respectively. The corresponding pair of model spectra is shown at the bottom of Fig. 2. To simulate PEY spectra, we summed up the intensity from the $4f^7$ channel and half of the intensity from the $4f^8 5(s,p)^{-1}$ channel. This allows us to obtain both the pre-edge and giant resonance structures in good agreement with experiments. Note that different channels produce photoelectrons with varying kinetic energies, depending on where the hole is created. In our case, the retarding voltage fully eliminates low-energy electrons produced by the $4f^n 4d^{-1}$ channel, while leaving high-energy electrons from the $4f^{n-1}$ channel unaffected. The other channels are either partially or fully cut depending on the selected voltage.

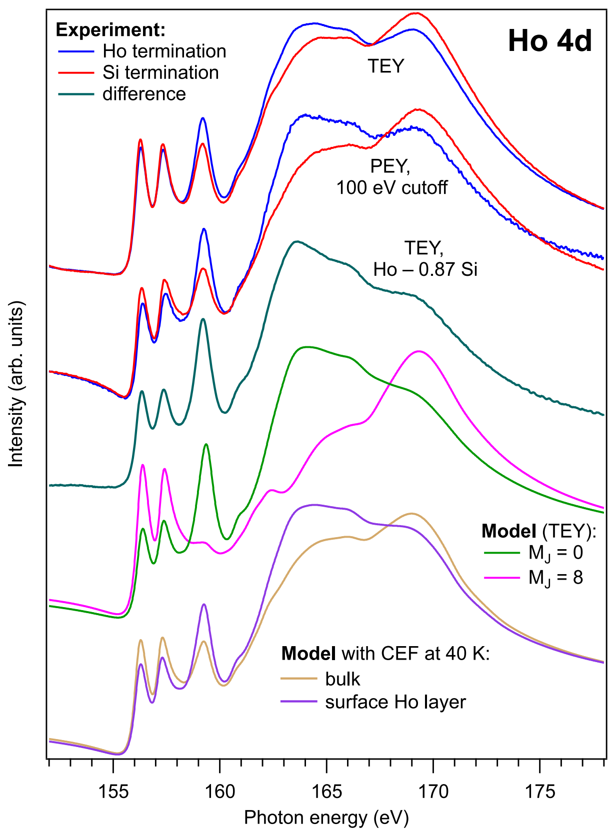

FIG. 3. Experimental XAS Ho $N_{4,5}$ spectra acquired in TEY and PEY regimes from Ho- and Si-terminated surfaces of PM $HoRh_2Si_2$ (at 40 K), compared with theoretical spectra for two hypothetical ground states $|0\rangle$ and $|8\rangle$ of Ho, as well as for more realistic states formed in CEF and described in the main text.

For heavy lanthanides, including Tb, a super-Coster-Kronig process mainly defines the shape of the giant resonance, which in turn can be used for estimating the orientation of Tb $4f$ moments, although several things should be kept in mind. First, PEY spectra were obtained by collecting electrons within a certain, not very large solid angle, whereas the calculated spectra are fully angle-integrated. Second, CEF may result in mixing of different $|M_J\rangle$ states. Third, excited states may contribute to the spectrum if the CEF splitting is comparable to kT. Therefore, only qualitative comparison is possible. In Fig. 2, we also present the spectrum labeled PEY, Tb–0.73 Si, illustrating the difference between the experimental PEY spectra obtained from Tb and Si surfaces with a scaling coefficient. The raw PEY spectrum from the Si termination is about 2.6 times less intense than that of the Tb surface due to attenuation of the measured Tb signal by a Si-Rh-Si surface block on the Si-terminated crystal. Thus, each atomic layer reduces the spectral intensity by the factor of about $2.6^{1/3} \approx 1/0.73$. We assume that the spectrum obtained from the Si-terminated surface closely resembles the spectrum

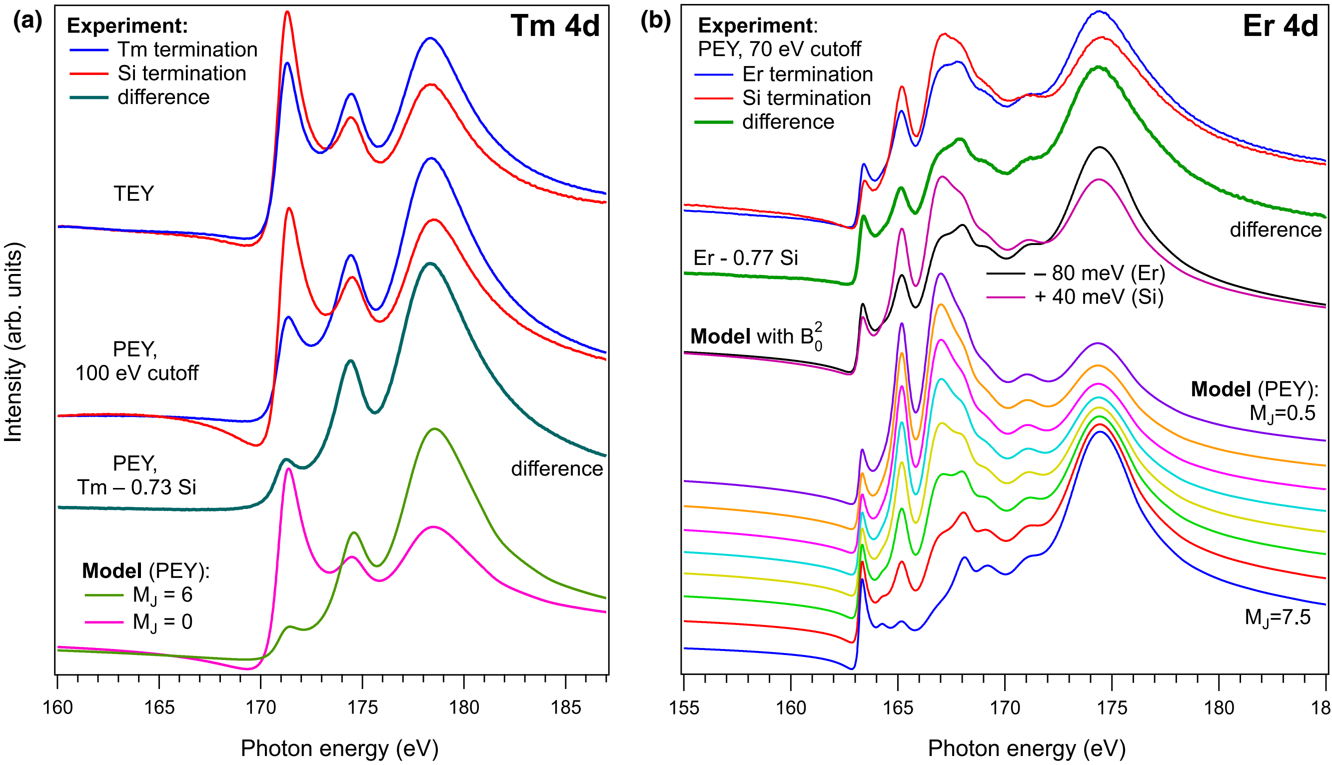

FIG. 4. (a) Experimental Tm $N_{4,5}$ XAS spectra acquired in TEY and PEY regimes from Tm- and Si-terminated surfaces of PM $TmRh_2Si_2$ at 40 K compared with theoretical spectra for two hypothetical ground states $|0\rangle$ and $|6\rangle$ of Tm. (b) Experimental and theoretical PEY spectra of $ErRh_2Si_2$ at 95 K, along with model spectra for different $|M_J\rangle$ states. For the calculated spectra, we summed up the intensity from the $4f^{n-1}$ and $4f^n5(s,p)^{-1}$ channels.

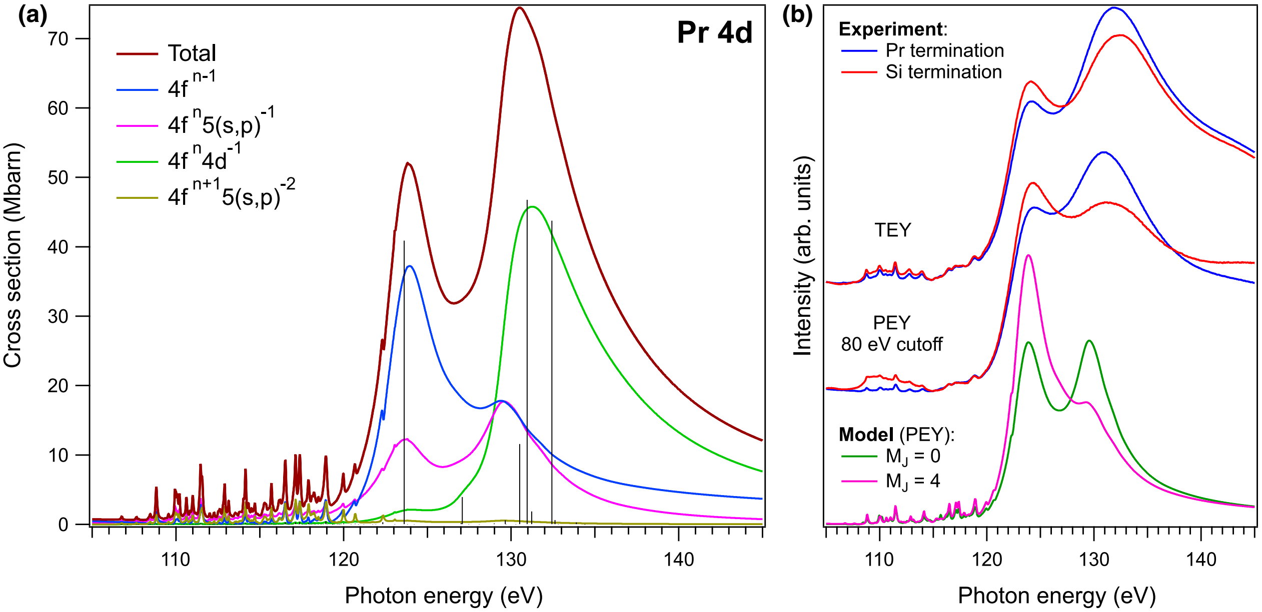

FIG. 5. (a) Theoretical XAS spectrum for Pr^{3+} at the $N_{4,5}$ threshold, along with contributions from different decay channels. (b) Experimental XAS spectra acquired in TEY and PEY regimes from Pr- and Si-terminated surfaces of PM $PrRh_2Si_2$ (at 95 K), compared with theoretical spectra for two hypothetical ground states $|0\rangle$ and $|4\rangle$ of Pr.

of the bulk. This is justified by similarity of TEY and PEY spectra for the Si surface and explained by the deep location of the Tb ions (fourth atomic layer below the Si surface). Then, we may conclude that the aforementioned difference spectrum should exclusively correspond to the topmost Tb layer on the Tb termination. Further comparison of this spectrum with the model spectra reveals that its shape closely resembles that computed for $M_J = 0$. This implies that the $4f$ moments of Tb at the surface (Tb termination) are locked within the surface plane, revealing an in-plane orientation, while in the bulk they are known to have an out-of-plane orientation (along the c axis). The latter is consistent with the observed similarity between the model spectrum with $M_J = 6$ and the XAS data for the Si termination.

The obtained XAS results are instructive, as they lead us to similar conclusions regarding the reorientation of the Tb $4f$ moments at the surface as previous $4f$ PE measurements [16]. Further, we consider a few more examples from the family of antiferromagnets LnRh$_2$Si$_2$ and the next material is HoRh$_2$Si$_2$ (T_N=27K). As we already mentioned, only TbRh$_2$Si$_2$ was in the AFM phase. All other samples were in the PM phase.

In Fig. 3, we present a summary of the experimentally obtained XAS Ho N$_{4,5}$ spectra taken from both Ho and Si surfaces, along with the simulated spectra. The strategy for the measurements was essentially the same for all systems considered here. For the freshly cleaved HoRh$_2$Si$_2$, we initially identified two large crystallites with Ho and Si surfaces using ARPES. Subsequently, XAS data were collected from each surface using both TEY and PEY regimes. Already a brief inspection of the TEY spectra shown at the top indicates that the line shape of the giant resonance exhibits strong changes when moving from the Ho to the Si surface. Additionally, some slight changes can be observed in the pre-edge structure. The spectral alterations become much stronger when we consider the PEY spectra taken with retarding voltage of 100 V. Next, we present the model spectra computed for the smallest $M_J = 0$ and largest $M_J = 8$ values. In the calculation, we took only the $4f^{n-1}$ and $4f^n 5(s,p)^{-1}$ channels to simulate PEY. Obviously, the model spectra differ much strongly than the experimental ones, indicating that the real states contributing to the spectra are quite far from those with maximal and minimal M_J. Nevertheless, qualitatively it is possible to say that for the Ho termination small M_J dominate in the ground state, while for the Si surface large M_J are significant.

It is worth noting that in Eq. (2) the terms with $A^*_{M_J} A_{M''_J}$ are zero if $|M_J - M''_J| > 2$. If the crystal has an n-fold symmetry ($n = 4$ for our systems), then in the PM phase the M_J values that form each $4f$ state may differ only by a number divisible by n. In this case, for $n > 2$ Eq. (2) reduces to

$$\sigma^{\nu} = \sum_{M_J} \left|A^{\nu}_{M_J}\right|^2 \sum_{J' q M'_J} \sigma_{J'} \frac{3(2J+1)}{2J'+1} \left|\varepsilon_q C^{J'M'_J}_{JM_J,1q}\right|^2. \qquad (5)$$

This expression indicates that the XAS spectrum is just a linear combination of the spectra for the pure $|M_J\rangle$ states. Hence, it is possible to estimate which $|M_J\rangle$ states dominate in the ground state by comparing the experimental spectrum with the calculated ones for different M_J. Examples of such spectra are given in the SM [33].

If there are estimations of the CEF parameters or coefficients A_{M_J}, it is possible to assess their accuracy through XAS measurements. In our previous study, we estimated the CEF parameters for both bulk and near-surface Ho layers in HoRh$_2$Si$_2$ [18]. At the bottom of Fig. 3, we show the modeled TEY spectrum reflecting the bulk, for which the CEF parameters were determined by fitting the calculated magnetic susceptibility and magnetization curves to the experimental data. As seen, this XAS spectrum closely resembles the experimental one taken from the Si termination. This is consistent with the assumption that the CEF in the Ho layer just below the Si-Rh-Si block should not differ significantly from the CEF in the bulk.

To analyze the properties of $4f$ moments in the topmost Ho layer for the Ho-terminated crystal, we performed a similar analysis to what was discussed for TbRh$_2$Si$_2$. Namely, we constructed the difference spectrum labeled Ho–0.87 Si, where the coefficient 0.87, reflecting the attenuation of the measured signal by the topmost Ho layer, is notably larger than that for the Tb case. This is because for the Ho case under discussion, we employed the TEY spectra, which are less surface sensitive than the PEY spectra used for the Tb case. As seen, the shape of the difference spectrum fits nicely to the model one calculated for $M_J = 0$. This suggests that $M_J = 0$ strongly predominates in the ground state of the surface Ho ions.

Now, let us discuss the XAS spectrum calculated solely for the topmost Ho layer, for which the CEF parameters were obtained by density functional theory (DFT) calculations [18]. Such calculations involve adjustable parameters, therefore the results should be experimentally verified. When comparing the difference spectrum with the theoretical one, it becomes apparent that their shapes do not match as closely as when comparing the experimental spectrum to the $M_J = 0$ modeled spectrum. Thus, the analysis of XAS data suggests that the CEF parameters obtained in our recent study [18] accurately describe the ground state of Ho in the bulk. However, for the topmost Ho layer, our DFT results seem to overestimate the contribution of the $|M_J\rangle$ states with $M_J \neq 0$.

It is useful to take a look at the respective lowest-energy states of Ho. From Ref. [18], for the bulk of HoRh$_2$Si$_2$, we have

$$|g^{1,2}\rangle = 0.86|\mp 7\rangle + 0.48|\mp 3\rangle + 0.12|\pm 1\rangle + 0.1|\pm 5\rangle,$$
$$|g^{3}\rangle = 0.58|-8\rangle + 0.38|-4\rangle + 0.2|0\rangle + 0.38|4\rangle + 0.58|8\rangle,$$

which represent the ground-state doublet and the next excited state at 0.4 meV. These states give the dominant contribution to the XAS spectrum at 40 K. For the top Ho layer of the Ho-terminated crystal, we have the following states that mostly define the XAS spectral shape:

$$|g^{1}\rangle = 0.48|-4\rangle + 0.73|0\rangle + 0.48|4\rangle,$$
$$|g^{2,3}\rangle = 0.11|\mp 7\rangle + 0.56|\mp 3\rangle + 0.73|\pm 1\rangle + 0.38|\pm 5\rangle,$$
$$|g^{4}\rangle = 0.23|-6\rangle + 0.67|-2\rangle + 0.67|2\rangle + 0.23|6\rangle,$$

that are the ground state, the excited doublet at 0.06 meV, and the next excited level at 0.12 meV. One can see that the states with different M_J are strongly mixed both for the bulk and surface Ho layers. However, for the bulk, the states with large M_J values dominate over those with small values. For the Ho surface, this is in the opposite way and in agreement with our qualitative conclusion made above.

Let us turn now to the AFM material TmRh$_2$Si$_2$, characterized by a relatively low Néel temperature of 6.4 K. For this system, XAS measurements were also conducted at 40 K, i.e., in the PM phase. For TmRh$_2$Si$_2$, we employed the same approach as for the Tb- and Ho-based systems, and the experimental results along with the model spectra are summarized in Fig. 4(a). The XAS data taken in TEY and PEY modes clearly indicate that the intensities of three spectral peaks are highly sensitive to the crystal surface, presented either by Tm or Si termination. From the PEY data we derived the difference spectrum, which is labeled Tm–0.73 Si and which reflects the properties of the topmost Tm layer on the Tm-terminated surface. When we compare this spectrum to the modeled spectra computed for the states with smallest $M_J = 0$ and largest $M_J = 6$, we observe that the intensities of the three peaks closely resemble those of the theoretical spectrum for $M_J = 6$. Thus, the Tm $4f$ moments are strongly influenced by the changes in CEF at the Tm surface. We may anticipate that in the magnetically ordered phase the moments should reorient from the primarily in-plane direction in the bulk to predominantly out-of-plane at the Tm surface.

For the next case, which will be $\mathrm{ErRh_2Si_2}$, and which also possesses a low Néel temperature of 12.8 K [46], we could perform the measurements only at essentially higher temperature, which was 95 K. The obtained data, including experimental results and modeling, are depicted in Fig. 4(b). In the top of Fig. 4(b), we show a pair of PEY spectra, which were taken from Er and Si terminations of $\mathrm{ErRh_2Si_2}$. The derived difference XAS spectrum, labeled Er– 0.77 Si, obviously resembles the spectrum computed for $M_J = 6.5$. We should mention, however, that even such a good agreement of their shape does not mean that this M_J value dominates in the ground state. Considering that the measurements were performed at a relatively high temperature of 95 K, it is important to note that different CEF-split $4f$ levels with various M_J values likely contribute to the spectrum. To further analyze the spectral shape, we use a simplified CEF model, neglecting all higher order CEF parameters besides B_0^2 [17,18]. In this case, we may write

$$\sigma = \frac{1}{Z}\sum_{M_J}\sigma_{M_J}\mathrm{e}^{-\frac{E_{M_J}}{kT}}, \quad E_{M_J} = tB_0^2 C_{JM_J,20}^{JM_J} \tag{6}$$

where σ_{M_J} are the spectra for pure $|M_J\rangle$ states, and the coefficient $t = \sqrt{7140}/525$ comes from the CEF matrix element for Er. By fitting the model difference spectrum to the experimental one, we estimate the CEF parameter $B_0^2 \approx -80\,\mathrm{meV}$ for the topmost Er layer on the Er termination. This value is quite close to our theoretical B_0^2 values of $-87\,\mathrm{meV}$ for Tb termination [17] and $-103\,\mathrm{meV}$ for Ho termination [18] estimated from DFT calculations. On the other hand, the spectrum from the Si termination is well described by $B_0^2 \approx 40\,\mathrm{meV}$, which is close to the value in the bulk of the other $\mathrm{LnRh_2Si_2}$ compounds with Tb, Dy, Ho and Yb [17,18,47]. Sign reversal of the B_0^2 parameter is expected to cause reorientation of the $4f$ moments at the surface in magnetically ordered phase [19].

Further, we turn to the case of $\mathrm{PrRh_2Si_2}$, where Pr serves as a representative of the light lanthanides group. Unlike heavy lanthanides, where the super Coster-Kronig decay channel is dominating, in light lanthanides there is a strong contribution of the f-tunneling process, which strongly affects the tail of the giant resonance. In Fig. 5(a), we present the XAS modeling results for Pr $4d \rightarrow 4f$ spectrum, along with partial cross sections. The green line represents the f-tunneling ($4f^n4d^{-1}$) decay channel, which exhibits a significantly stronger contribution as compared to the cases of Tb, Ho, Er, and Tm.

Now, let us consider the results of XAS measurements performed on $\mathrm{PrRh_2Si_2}$ and the corresponding modeling, which are shown in Fig. 5(b). The top pair of spectra were taken in TEY mode from the Pr and Si surfaces of a freshly cleaved sample. Their difference, especially in the region of the giant resonance, is notable. The next pair of XAS spectra were obtained from both surface terminations with a retarding voltage of 80 V. As seen, the aforementioned difference becomes significantly more pronounced. Additionally, certain differences can be observed in the pre-edge structure, particularly noticeable for the Si termination. We assume that their emergence may be related to the influence of the valence states of Si atoms that may interact and hybridize with the Pr $4f$ orbitals, but this aspect will not be further discussed. For modeling, as in the previous cases, we considered the largest and smallest M_J values for Pr^{3+} that are 0 and 4, and the pair of respective spectra is shown at the bottom of Fig. 5(b). Comparing the line shape of the giant resonance, that is formed mainly by two peaks, we see that the relative intensity differences for these two peaks observed experimentally are qualitatively reproduced in the calculated spectra, indicating strong differences in the Pr $4f$ ground state at the surface. Our observation is consistent with the out-of-plane orientation of moments in the AFM phase [48]. However, the peaks in experiment are much broader than in the calculations. We tentatively assign this broadening to the already mentioned hybridization of $4f$ and other valence states and to possible contribution of interatomic photoexcitation and decay processes.

The results obtained for Pr are quite instructive for discussing the case of Ce. This is because the giant resonance of Ce at the $4d \rightarrow 4f$ threshold is often utilized in photoemission measurements, aiming to highlight the admixture of Ce-$4f$ states to the valence bands, particularly in the Fermi level region, and to enhance the Kondo peak. Our results suggest that since the line shape of the giant resonance is sensitive to the specific ground M_J state, performing a thorough analysis of the line shape of XAS Ce $4d \rightarrow 4f$ for the material under consideration, followed by subsequent resonant ARPES measurements, could provide deeper insight into the Kondo physics linked with the orientation of Ce $4f$ moments in the bulk and at the surface. This subject will be the focus of our next studies.

To summarize, we performed systematic XAS measurements at the Ln $4d$ edge on layered antiferromagnets $\mathrm{LnRh_2Si_2}$. We examined their Si- and Ln-terminated surfaces, performing the measurements in surface-sensitive PEY and bulk-sensitive TEY regimes. For a comprehensive analysis of the obtained XAS spectra, we performed detailed modeling to evaluate the contributions from different channels of core-hole decay to the lineshape of pre-edge and giant resonance regions. The analysis of both experimental and modeled XAS spectra indicates significant alterations in the ground state of lanthanides near the surface, potentially leading to the reorientation of their $4f$ moments, attributed to changes in CEF. The derived conclusions agree perfectly with those obtained from other techniques, particularly from $4f$ photoemission measurements [16–18]. It is important to note that the value of the CEF splitting, and particularly between the ground state and the first excited state, along with the temperature of XAS measurements, may significantly affect the analysis. Due to involvement of various CEF-split $4f$ levels, different $|M_J\rangle$ states may contribute to the spectrum, thereby introducing complexities into the analysis.

Our experimental findings together with the modeled XAS spectra at the Ln $4d$ edge, including those for individual $|M_J\rangle$ states, significantly enhance the capability for analysis of electronic and magnetic properties of lanthanide-based systems. The presented results and database of modeled Ln $4d$ XAS spectra for all lanthanides (given in the SM [33]) will also facilitate magnetic dichroism experiments in both surface- and bulk-sensitive regimes.

ACKNOWLEDGMENTS

We acknowledge the German Research Foundation (DFG) for the support of our research through Grants No. GU 2228/2-1 (Project No. 512344412), No. SFB1143 (Project No. 247310070), and No. TRR288 (No. 422213477, Project No. A03). The authors acknowledge St. Petersburg State University for Research Project No. 95442847. The work of V.S.S. (analysis of experimental XAS data) and D.Y.U. (modeling of XAS spectra) was supported by the Ministry of Science and Higher Education of the Russian Federation (No. 075-15-2024-632). Additional funding was provided from the Diputación Foral de Gipuzkoa “Gipuzkoa Quantum” program (No. DFG-QUAN-000029). We acknowledge MAX IV Laboratory for experimental time on FlexPES beamline [27] under Proposal No. 20230457. Research conducted at MAX IV, a Swedish national user facility, is supported by the Swedish Research Council under Contract No. 2018-07152, the Swedish Governmental Agency for Innovation Systems under Contract No. 2018-04969, and Formas under Contract No. 2019-0249. We are grateful for the expert scientific and technical support provided by Alexei Preobrajenski and Alexander Generalov during the experiment at FlexPES [27], as well as for valuable discussions while working on this paper.

[1] J.-C. G. Bünzli, Lanthanide luminescence for biomedical analyses and imaging, Chem. Rev. **110**, 2729 (2010).

[2] W. Hou, G. Wang, X. Wu, S. Sun, C. Zhao, W.-S. Liu, and F. Pan, Lanthanide clusters as highly efficient catalysts regarding carbon dioxide activation, New J. Chem. **44**, 5019 (2020).

[3] X. Z. Li, C.-B. Tian, and Q.-F. Sun, Coordination-directed self-assembly of functional polynuclear lanthanide supramolecular architectures, Chem. Rev. **122**, 6374 (2022).

[4] L. Yang, J. Luo, L. Gao, B. Song, and J. Tang, Inorganic lanthanide compounds with f–d transition: From materials to electroluminescence devices, J. Phys. Chem. Lett. **13**, 4365 (2022).

[5] L. Wang, P. Fang, Z. Zhao, Y. Huang, Z. Liu, and Z. Bian, Rare earth complexes with $5d$–$4f$ transition: New emitters in organic light-emitting diodes, J. Phys. Chem. Lett. **13**, 2686 (2022).

[6] D. N. Woodruff, R. E. P. Winpenny, and R. A. Layfield, Lanthanide single-molecule magnets, Chem. Rev. **113**, 5110 (2013).

[7] V. D. Dergachev, D. D. Nakritskaia, and S. A. Varganov, Strong relativistic effects in lanthanide-based single-molecule magnets, J. Phys. Chem. Lett. **13**, 6749 (2022).

[8] M. Shimozawa, S. K. Goh, R. Endo, R. Kobayashi, T. Watashige, Y. Mizukami, H. Ikeda, H. Shishido, Y. Yanase, T. Terashima, T. Shibauchi, and Y. Matsuda, Controllable Rashba spin-orbit interaction in artificially engineered superlattices involving the heavy-fermion superconductor $\mathrm{CeCoIn_5}$, Phys. Rev. Lett. **112**, 156404 (2014).

[9] *Novel Functional Magnetic Materials*, Springer Series in Materials Science, edited by A. Zhukov (Springer International Publishing, Cham, Switzerland, 2016).

[10] S. Fahrendorf, N. Atodiresei, C. Besson, V. Caciuc, F. Matthes, S. Blügel, P. Kögerler, D. E. Bürgler, and C. M. Schneider, Accessing $4f$-states in single-molecule spintronics, Nat. Commun. **4**, 2425 (2013).

[11] *Lanthanide-Based Multifunctional Materials: From OLEDs to SIMs*, Advanced Nanomaterials, edited by P. Martín-Ramos and M. Ramos Silva (Elsevier, Amsterdam, Netherlands, 2018).

[12] *Novel Magnetic Nanostructures: Unique Properties and Applications*, Advanced Nanomaterials, edited by M. C. Natalia Domracheva and E. Rentschler (Elsevier, Amsterdam, Netherlands, 2018).

[13] S. Li, L. Zhou, T. Frauenheim, and J. He, Light-controlled ultrafast magnetic state transition in antiferromagnetic–ferromagnetic van der Waals heterostructures, J. Phys. Chem. Lett. **13**, 6223 (2022).

[14] B. C. Mummaneni, J. Liu, G. Lefkidis, and W. Hübner, Laser-controlled implementation of controlled-not, Hadamard, swap, and Pauli gates as well as generation of Bell states in a $3d$–$4f$ molecular magnet, J. Phys. Chem. Lett. **13**, 2479 (2022).

[15] F. Huttmann, N. Rothenbach, S. Kraus, K. Ollefs, L. M. Arruda, M. Bernien, D. Thonnig, A. Delin, J. Fransson, K. Kummer, N. B. Brookes, O. Eriksson, W. Kuch, T. Michley, and H. Wende, Europium cyclooctatetraene nanowire carpets: A low-dimensional, organometallic, and ferromagnetic insulator, J. Phys. Chem. Lett. **10**, 911 (2019).

[16] D. Y. Usachov, D. Glazkova, A. V. Tarasov, S. Schulz, G. Poelchen, K. A. Bokai, O. Y. Vilkov, P. Dudin, K. Kummer, K. Kliemt, C. Krellner, and D. V. Vyalikh, Estimating the orientation of $4f$ magnetic moments by classical photoemission, J. Phys. Chem. Lett. **13**, 7861 (2022).

[17] A. V. Tarasov, D. Glazkova, S. Schulz, G. Poelchen, K. Kliemt, A. Kraiker, M. Muntwiler, C. Laubschat, A. Generalov, C. Polley, C. Krellner, D. V. Vyalikh, and D. Y. Usachov, Crystal electric field and properties of $4f$ magnetic moments at the surface of the rare-earth compound $\mathrm{TbRh_2Si_2}$, Phys. Rev. B **106**, 155136 (2022).

[18] D. Y. Usachov, A. V. Tarasov, D. Glazkova, M. Mende, S. Schulz, G. Poelchen, A. V. Fedorov, O. Y. Vilkov, K. A. Bokai, V. S. Stolyarov, K. Kliemt, C. Krellner, and D. V. Vyalikh,

Insight into the temperature-dependent canting of 4*f* magnetic moments from 4*f* photoemission, J. Phys. Chem. Lett. **14**, 5537 (2023).

[19] H. Tsuchiura, T. Yoshioka, and P. Novák, Bridging atomistic magnetism and coercivity in Nd-Fe-B magnets, Scr. Mater. **154**, 248 (2018).

[20] H. Tsuchiura, T. Yoshioka, P. Novák, J. Fischbacher, A. Kovacs, and T. Schrefl, First-principles calculations of magnetic properties for analysis of magnetization processes in rare-earth permanent magnets, Sci. Technol. Adv. Mater. **22**, 748 (2021).

[21] H. Tsuchiura, T. Yoshioka, and P. Novák, First-principles calculations of crystal field parameters of Nd ions near surfaces and interfaces in Nd-Fe-B magnets, IEEE Trans. Magn. **50**, 1 (2014).

[22] P. Hansmann, A. Severing, Z. Hu, M. W. Haverkort, C. F. Chang, S. Klein, A. Tanaka, H. H. Hsieh, H.-J. Lin, C. T. Chen, B. Fåk, P. Lejay, and L. H. Tjeng, Determining the crystal-field ground state in rare earth heavy fermion materials using soft-x-ray absorption spectroscopy, Phys. Rev. Lett. **100**, 066405 (2008).

[23] T. Willers, B. Fåk, N. Hollmann, P. O. Körner, Z. Hu, A. Tanaka, D. Schmitz, M. Enderle, G. Lapertot, L. H. Tjeng, and A. Severing, Crystal-field ground state of the noncentrosymmetric superconductor CePt$_3$Si: A combined polarized soft x-ray absorption and polarized neutron study, Phys. Rev. B **80**, 115106 (2009).

[24] F. Strigari, T. Willers, Y. Muro, K. Yutani, T. Takabatake, Z. Hu, Y.-Y. Chin, S. Agrestini, H.-J. Lin, C. T. Chen, A. Tanaka, M. W. Haverkort, L. H. Tjeng, and A. Severing, Crystal-field ground state of the orthorhombic Kondo insulator CeRu$_2$Al$_{10}$, Phys. Rev. B **86**, 081105(R) (2012).

[25] H. Ogasawara and A. Kotani, Calculation of rare-earth 4*d* giant-absorption spectra with multiplet effects and decay processes, J. Synchrotron Rad. **8**, 220 (2001).

[26] G. Poelchen, I. P. Rusinov, S. Schulz, M. Güttler, M. Mende, A. Generalov, D. Y. Usachov, S. Danzenbächer, J. Hellwig, M. Peters, K. Kliemt, Y. Kucherenko, V. N. Antonov, C. Laubschat, E. V. Chulkov, A. Ernst, K. Kummer, C. Krellner, and D. V. Vyalikh, Interlayer coupling of a two-dimensional Kondo lattice with a ferromagnetic surface in the antiferromagnet CeCo$_2$P$_2$, ACS Nano **16**, 3573 (2022).

[27] A. Preobrajenski, A. Generalov, G. Öhrwall, M. Tchaplyguine, H. Tarawneh, S. Appelfeller, E. Frampton, and N. Walsh, FlexPES: A versatile soft X-ray beamline at MAX IV Laboratory, J. Synchrotron Rad. **30**, 831 (2023).

[28] K. Kliemt, M. Peters, F. Feldmann, A. Kraiker, D.-M. Tran, S. Rongstock, J. Hellwig, S. Witt, M. Bolte, and C. Krellner, Crystal growth of materials with the ThCr$_2$Si$_2$ structure type, Cryst. Res. Technol. **55**, 1900116 (2020).

[29] M. Güttler, K. Kummer, S. Patil, M. Höppner, A. Hannaske, S. Danzenbächer, M. Shi, M. Radovic, E. Rienks, C. Laubschat, C. Geibel, and D. V. Vyalikh, Tracing the localization of 4*f* electrons: Angle-resolved photoemission on YbCo$_2$Si$_2$, the stable trivalent counterpart of the heavy-fermion YbRh$_2$Si$_2$, Phys. Rev. B **90**, 195138 (2014).

[30] D. Y. Usachov, I. A. Nechaev, G. Poelchen, M. Güttler, E. E. Krasovskii, S. Schulz, A. Generalov, K. Kliemt, A. Kraiker, C. Krellner, K. Kummer, S. Danzenbächer, C. Laubschat, A. P. Weber, J. Sánchez-Barriga, E. V. Chulkov, A. F. Santander-Syro, T. Imai, K. Miyamoto, T. Okuda *et al.*, Cubic Rashba effect in the surface spin structure of rare-earth ternary materials, Phys. Rev. Lett. **124**, 237202 (2020).

[31] M. Güttler, A. Generalov, M. M. Otrokov, K. Kummer, K. Kliemt, A. Fedorov, A. Chikina, S. Danzenbächer, S. Schulz, E. V. Chulkov, Y. M. Koroteev, N. Caroca-Canales, M. Shi, M. Radovic, C. Geibel, C. Laubschat, P. Dudin, T. K. Kim, M. Hoesch, C. Krellner *et al.*, Robust and tunable itinerant ferromagnetism at the silicon surface of the antiferromagnet GdRh$_2$Si$_2$, Sci. Rep. **6**, 24254 (2016).

[32] A. Generalov, M. M. Otrokov, A. Chikina, K. Kliemt, K. Kummer, M. Höppner, M. Güttler, S. Seiro, A. Fedorov, S. Schulz, S. Danzenbächer, E. V. Chulkov, C. Geibel, C. Laubschat, P. Dudin, M. Hoesch, T. Kim, M. Radovic, M. Shi, N. C. Plumb *et al.*, Spin orientation of two-dimensional electrons driven by temperature-tunable competition of spin-orbit and exchange-magnetic interactions, Nano Lett. **17**, 811 (2017).

[33] See Supplemental Material at http://link.aps.org/supplemental/10.1103/PhysRevB.110.075157 for theoretical XAS spectra and details of calculations.

[34] C. G. Olson and D. W. Lynch, Rare-earth 4*d* absorption spectra in rare-earth trifluorides, J. Opt. Soc. Am. **72**, 88 (1982); T. M. Zimkina, V. A. Fomichev, S. A. Gribovskii, and I. I. Zhukova, Anomalies in the character of the x-ray absorption of rare-earth elements of the lanthanide group, Fiz. Tverd. Tela **9**, 1447 (1967) [Sov. Phys. Solid State **9**, 1128 (1967)].

[35] K. T. Moore, B. W. Chung, S. A. Morton, A. J. Schwartz, J. G. Tobin, S. Lazar, F. D. Tichelaar, H. W. Zandbergen, P. Söderlind, and G. van der Laan, Changes in the electronic structure of cerium due to variations in close packing, Phys. Rev. B **69**, 193104 (2004).

[36] J. L. Dehmer, A. F. Starace, U. Fano, J. Sugar, and J. W. Cooper, Raising of discrete levels into the far continuum, Phys. Rev. Lett. **26**, 1521 (1971).

[37] A. F. Starace, Potential-barrier effects in photoabsorption. I. General theory, Phys. Rev. B **5**, 1773 (1972).

[38] J. Sugar, Potential-barrier effects in photoabsorption. II. Interpretation of photoabsorption resonances in lanthanide metals at the 4*d*-electron threshold, Phys. Rev. B **5**, 1785 (1972).

[39] M. Richter, M. Meyer, M. Pahler, T. Prescher, E. v. Raven, B. Sonntag, and H.-E. Wetzel, Experimental study of atomic 4*d* giant resonances by photoabsorption and photoelectron spectroscopy: Sm, Eu, and Gd, Phys. Rev. A **40**, 7007 (1989).

[40] J. E. Prieto, O. Krupin, K. Doebrich, F. Heigl, G. Kaindl, and K. Starke, X-ray magneto-optics of lanthanide materials: Principles and applications, Appl. Phys. A **80**, 1021 (2005).

[41] K. Starke, Z. Hu, F. Hübinger, E. Navas, G. Kaindl, and G. van der Laan, Magnetic circular dichroism in lanthanide 4*d*-4*f* giant resonant photoemission: Terbium, Eur. Phys. J. B **12**, 171 (1999).

[42] B. T. Thole, P. Carra, F. Sette, and G. van der Laan, X-ray circular dichroism as a probe of orbital magnetization, Phys. Rev. Lett. **68**, 1943 (1992).

[43] M. Altarelli, Sum rules for x-ray magnetic circular dichroism, Il Nuovo Cimento D **20**, 1067 (1998).

[44] G. Bihlmayer, P. Noël, D. V. Vyalikh, E. V. Chulkov, and A. Manchon, Rashba-like physics in condensed matter, Nat. Rev. Phys. **4**, 642 (2022).

[45] S. Quezel, J. Rossat-Mignod, B. Chevalier, P. Lejay, and J. Etourneau, Magnetic ordering in $TbRh_2Si_2$ and $CeRh_2Si_2$, Solid State Commun. **49**, 685 (1984).

[46] A. Szytuła, M. Ślaski, H. Ptasiewicz-Bąk, J. Leciejewicz, and A. Zygmunt, Magnetic ordering in $NdRh_2Si_2$ and $ErRh_2Si_2$, Solid State Commun. **52**, 395 (1984).

[47] A. S. Kutuzov and A. M. Skvortsova, Crystal electric field parameters for Yb^{3+} ion in $YbRh_2Si_2$, J. Phys.: Conf. Ser. **324**, 012039 (2011).

[48] A. Szytuła, D. Kaczorowski, Ł. Gondek, A. Arulraj, S. Baran, and B. Penc, Magnetic structure of $PrRh_2Si_2$, Solid State Commun. **146**, 61 (2008).